Plasmonics
https://doi.org/10.1007/s11468-023-02035-0

RESEARCH

A Portable Plasmonic Biosensor Kit for Diagnostics of Sexually Transmitted Infection

Arif E. Cetin[1]

Received: 23 August 2023 / Accepted: 1 September 2023

Abstract
Sexually transmitted infections (STIs) due to Neisseria gonorrhoeae (NG) and Chlamydia trachomatis (CT) pose global health challenges due to their widespread prevalence through sexual contact. Rapid and user-friendly diagnostic solutions are crucial to curb their spread and mitigate potential complications. In this article, we introduced a portable plasmonic biosensor kit for the detection of NG and CT bacteria in urine samples. Our platform merges label-free plasmonic nanohole sensing with lens-free computational imaging, revolutionizing point-of-care pathogen diagnosis. The system captures and analyzes diffraction field images, uncovering subtle bacterial presence cues. With a low-cost pump compartment and flow cell, we ensured precise sample delivery to the plasmonic chip. The system software controls hardware setup, test execution, and image analysis for bacterial detection. Leveraging control and sensor antibodies, our technology excels in sensitivity and selectivity. Microfluidic channels with multiple sensor locations enable separate NG and CT testing. Our imaging-based approach allows simultaneous detection, obviating the need for separate assays. Integrating multiple sensor sites ensures robust high-throughput testing. Employing plasmonic pixels for control tests effectively mitigates the background noise. Simple optics, affordable components, and controlled environment underscore the practicality of our handheld biosensor. Strong detection limits, e.g., 452 CFU/mL for NG and 121 CFU/mL for CT bacteria (CFU: colony-forming unit), position our technology as a transformative point-of-care diagnostic tool for pathogenic diseases, bridging accessibility and affordability gaps.

Keywords Point-of-care diagnostics · Pathogen detection · Lensfree imaging · Label-free biosensing · Plasmonics · Nanotechnology

Introduction

Instances of infections transmitted via sexual contact represent one of the prevailing and extensively disseminated afflictions globally [1]. The most common STIs are chlamydia, gonorrhea, syphilis, and HIV [2]. Amid this spectrum, ailments spawned by Neisseria gonorrhoeae (NG) and Chlamydia trachomatis (CT) emerge as the foremost and secondary most recorded bacterial infections, boasting almost one million fresh instances on a daily basis [3]. Despite the possibility of effective remedy, a substantial proportion of these infections manifest no symptoms, and numerous individuals remain unassessed and unattended within an appropriate timeframe. This could subsequently pave the way for enduring consequences like barrenness, inflammations of the pelvic region, pregnancies occurring outside the uterus, or persistent pelvic discomfort [4]. The contemporary customary methodologies for identifying NG and CT bacteria hinge upon nucleic acid amplification tests (NAATs), necessitating specialized laboratory environments and preliminary treatment procedures for samples (such as cellular breakdown or DNA extraction) [5, 6]. This makes it difficult to diagnose and treat these infections in resource-limited settings. A rapid and simple diagnostic test for NG and CT bacteria would be a major improvement. This test would be easy to use and could be performed in a doctor's office or clinic. It would also be affordable, making it accessible to people in resource-limited settings. A rapid and simple diagnostic test for these bacteria would have a number of benefits. It would improve early detection of these infections, which would lead to better health

✉ Arif E. Cetin
arifengin.cetin@ibg.edu.tr

[1] Izmir Biomedicine and Genome Center, Balcova, Izmir 35340, Turkey

Published online: 06 September 2023

outcomes for patients. It would also increase access to treatment for these infections, which would help to reduce the spread of the infections. Additionally, a rapid and simple diagnostic test would be less expensive than the current methods, which would reduce the financial burden on patients and healthcare systems.

In this respect, biosensor technologies without reliance on optical/chemical labels have introduced fresh perspectives into the realm of diagnosing contagious ailments [7]. These methods prove particularly advantageous for on-the-spot diagnostic applications due to their capacity to circumvent the necessity for optical or radioactive markers, as well as enzymatic catalysts. These conventional markers suffer from the intrusion of mutual interference between labels and other molecular binding occurrences. Furthermore, they surmount challenges stemming from limited marker quantities, along with protracted and intricate labeling procedures. Within existing literature, three primary modes of signal transduction have been advanced, namely optical [8], electrical [9], and mechanical[10] mechanisms, all striving to generate information devoid of labeling. Among these, optical biosensors enjoy pronounced prominence owing to their aptitude in fostering interactions between light and matter, resulting in robust sensory signals that external detectors can promptly decipher. This attribute grants optical biosensors a distinctive edge over alternative methodologies, as they boast the capability to facilitate remote signal transduction through the establishment of light-matter interaction. This dynamic yields compelling sensory cues, all without necessitating direct physical contact with the targeted analytes [8]. Nevertheless, the cultivation of precise and dependable sensory signals necessitates robust light-matter interaction. Achieving this hinges upon systems that intricately align light with the analytes of interest [11]. Consequently, a majority of optical biosensor solutions make use of unwieldy and costly instruments, a circumstance that poses limitations for deploying them effectively in portable, real-world, point-of-care diagnostics.

Lately, subwavelength nanohole arrays have emerged as a potent contender for the arena of analyses conducted at the point of need. Their extraordinary capacity to constrain light under usual illumination conditions has rendered them an appealing prospect. This unique geometrical attribute substantially streamlines the process of optical alignment, a pivotal aspect when aiming to actualize biosensing systems that are resilient and portable for field applications [12]. This distinct collinear configuration also furnishes the opportunity for signal assessment via imaging apparatus in an array configuration, such as CCD (charge-coupled device) or CMOS (complementary metal-oxide semiconductor) cameras. This, in contrast to conventional employment of photodetectors or spectrometers, ushers in the potential for multiplexed and high-throughput biosensing [13]. Operating within a restricted spectral range and adept at selectively transmitting specific wavelengths while filtering out the rest, nanohole arrays possess the inherent capability to yield sensory signals boasting elevated signal-to-noise ratios [14]. Notably, recent strides have also harnessed plasmonic nanoholes to achieve the detection of pathogens, including viruses and bacteria [15]. Despite the success they exhibit in pathogen detection sans labels, biosensors exploiting nanohole arrays remain hinged upon laboratory-grade equipment. Regrettably, this dependence significantly curtails their suitability for utilization within resource-poor contexts. Thus, the clarion call resounds for cost-effective, field-adaptable plasmonic platforms tailored for label-free pathogen detection [16].

Along this line, the demand persists for biosensors that can be deployed in the field, enabling efficient biosensing without the reliance on optical labels [17, 18]. To address this challenge, we introduced a handheld, lens-free plasmonic biosensor that amalgamates plasmonic nanohole arrays with computational on-chip imaging to identify ultrathin layers of protein complexes [19]. This approach could facilitate simultaneous detection of diverse protein molecules, making it suitable for multiplexing applications. Moreover, it enables the quantification of varying protein concentrations, ensuring reliability in high-throughput applications. Our innovative approach found successful application in virus detection, showcasing its potential in disease diagnosis within field conditions [20]. Through combining this plasmonic read-out technique with a microfluidic chamber and an externally attached syringe pump setup, we achieved real-time tracking of simultaneous binding events among protein molecules on the surface of a plasmonic chip, distinguished by its periodic nanohole architecture [21].

In this article, we introduced an advanced iteration of our handheld technology, presenting it as a plasmonic biosensor kit designed for the simultaneous detection of Neisseria gonorrhoeae (NG) and Chlamydia trachomatis (CT) in urine samples. This novel platform builds upon the foundation of our previously demonstrated technologies, integrating label-free sensing based on plasmonic nanoholes and lens-free computational imaging. This integration empowers point-of-care diagnosis for sexually transmitted diseases due to multiple pathogenic agents. The system captures and analyzes diffraction field images, extracting key information from variations related to bacteria presence. Unlike our previous works based on bulky pump settings, incorporating a cost-effective piezo pump compartment and a versatile flow cell, the technology achieves precise sample delivery to the plasmonic chip surface. In contrast to our earlier real-time measurement approach using microfluidics, this technology leverages the microfluidic flow cell to functionalize the plasmonic chip's surface with diverse surface modifications, e.g., antibiotics and agents, as well as the capture of bacteria. This surface modification modality enhances the

likelihood of bacteria capture, especially in scenarios with low pathogen concentrations. The technology is supported by a software suite that enables hardware configuration, test execution, and image analysis to determine bacterial presence in urine samples. Beyond the utilization of sensor antibodies, our technology also incorporates control antibodies, a strategic measure aimed at ensuring elevated sensitivity and specificity in the detection of bacteria. The use of distinct microfluidic channels with multiple sensor locations allows separate testing for each bacteria type. Through an imaging-based methodology, our technology can simultaneously detect NG and CT bacteria on a single platform, negating the need for separate tests. The incorporation of multiple sensor locations in the microfluidic channels enables high-throughput testing of the same target bacteria, ensuring test reliability. The platform also utilizes multiple plasmonic pixels for control tests, eliminating signals stemming from biological, mechanical, or optical noise. The system employs straightforward optics with affordable components, arranged within a controlled environment without necessitating optical or mechanical instrumentation. With a compact and lightweight design with impressive limit of detection, e.g., 452 CFU/mL for NG and 121 CFU/mL for CT bacteria (CFU: colony-forming unit), our handheld biosensor stands as a robust contender for point-of-care diagnostics in the realm of pathogenic diseases.

Various approaches have been utilized in the literature to detect NG and CT bacteria. For instance, Chen et al. showed a detection limit of 50 copies per test for these bacteria strains via thermal amplification in an isothermal environment, along with a lateral flow biosensor employing gold nanoparticles [22]. Wang et al. demonstrated a detection limit of 50 CFU/mL using surface plasmon resonance (SPR) biosensors, while incorporating magnetic nanoparticle assays for the detection of Escherichia coli [23]. Zhai et al. introduced a multiplex recombinase polymerase amplification-lateral flow detection (RPA-LFD) assay yielding, ~ 86% and ~ 91% sensitivity for the detection of NG and CT bacteria. However, these methods necessitate the inclusion of pretreatment of samples or subsequent amplification steps. Cui et al. introduced quantum dots immunofluorescence biosensors employing optical fiber probes for Staphylococcus aureus detection with an LoD of 10^3 CFU/mL [24]. Detection methods employing bacteriophages have shown promising potential with lower limits of detection (LoD) reaching as low as 10 CFU/mL [25]. In the context of bacteria detection, achieving multiplexed and label-free detection of bacteria at physiologically relevant concentrations holds paramount importance. In that sense, Yoo et al. presented a novel approach involving an aptamer-functionalized localized surface plasmon resonance sensor for the simultaneous detection of various bacteria strains, demonstrating 10^4 CFU/mL detection limits in standard buffer conditions [26]. Soler et al. demonstrated the successful detection of these bacteria directly from urine samples, achieving a detection limit of 1500 CFU/mL for NG and 300 CFU/mL for CT bacteria [27]. In this context, our technology marks a notable advancement in terms of detection limits, delivering better sensitivity for detecting both bacterial strains in urine. A distinctive feature of our approach is the utilization of a camera-based sensing scheme, which sets us apart from the conventional spectroscopic read-out method for the detection of bacteria shown in the literature mentioned here. Unlike the sequential monitoring required by the sensor locations on the plasmonic chip in the spectroscopic approach, our camera-based scheme enables simultaneous detection for multiplexing modality. Our read-out scheme, designed for multiple monitoring of sensor locations, notably enhances the system's throughput. This enhancement plays a pivotal role in strengthening test reliability, a crucial facet of our technology.

Materials and Methods

Handheld Plasmonic Biosensor Kit

Figure 1A, B show the photographs and the schematics of the plasmonic system, respectively. In order to aid the attainment of the diffraction field images by decreasing ambient disturbances and background noises, and combining all machinery constituents, we engineered a housing via 3D-printing technology. This enclosure furnishes a shaded milieu for optimal imaging environment. The setup encompasses four primary elements: (i) plasmonic chip, (ii) sample preparation module, (iii) imaging module, and (iv) software module. The plasmonic chip incorporates a thin gold film textured with nanohole lattices. The surface of the plasmonic chip is modified with capturing antibodies possessing high affinities for NG and CT bacteria. In the imaging module, an LED (light-emitting-diode) source illuminates the plasmonic chip, while a CMOS camera (complementary metal oxide semiconductor) captured the conveyed light, thereby monitoring the diffractive field patterns formed by the plasmonic nanoholes. The intensity variations in the plasmonic chip are used to determine the presence of bacteria in the targeted samples. The sample preparation module merges a polydimethylsiloxane (PDMS)-based flow cell and a piezoelectric pump unit, which facilitates the meticulous delivery of samples to the sensing surface, enabling the perfect capture of the targeted bacteria by the antibodies on the plasmonic chip surface. This module partitions the plasmonic microarray into four distinct segments: a pair of sensor regions for NG and CT bacteria, and an additional pair of control regions, with one functionalized with a control antibody while the other remains unaltered. Within the boundaries of the sensor

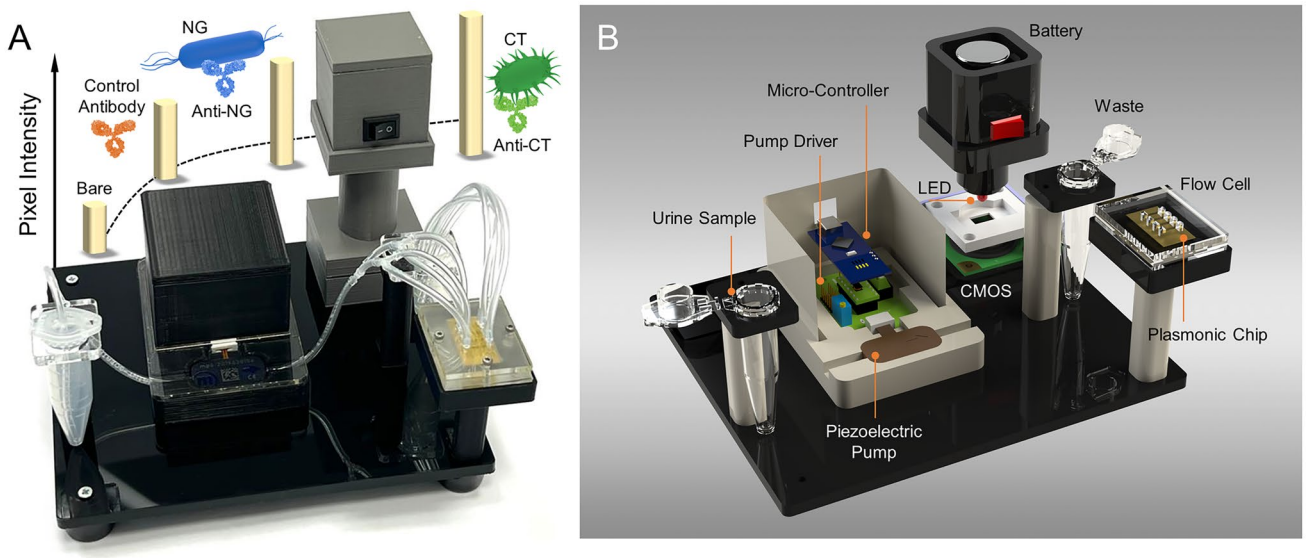

Fig. 1 **A** Photograph and **B** schematics of the portable biosensor kit

compartments, a bioreactive monolayer is established, enriched with specific antibodies tailored for the detection of NG and CT bacteria. In contrast, the control compartments serve the purpose of detecting observable alterations arising from biological, optical, or mechanical deviations. The software module encompasses a graphical user interface (GUI) that streamlines simultaneous authority over the optical and microfluidic hardware constituents. Furthermore, it integrates an image-processing algorithm that employs plasmonic diffraction field images to determine the presence of bacteria in urine samples. System supervision is executed by means of a notebook, wherein the correspondence between imaging and sample preparation units is actualized through USB (universal serial bus).

Plasmonic Chip

The plasmonic chip comprises periodic arrays of nanoholes, with a diameter of 200 nm and a periodicity of 550 nm. Figure 2A shows the schematic illustration of the fabrication method. The fabrication of the apertures was conducted on a 120 nm thick gold (Au) film. The creation of the nanohole arrays was executed employing a high-throughput fabrication method based on deep-ultraviolet (deep-UV) lithography. The supporting substrate employed for the fabrication procedure was a 4-inch fused silica wafer possessing a thickness of 500 µm, coated with a 100 nm layer of LPCVD-SiN (low-pressure chemical vapor deposition-silicon nitride). The initial steps involved the deposition of a 5 nm layer of chromium (Cr) serving as an adhesion layer, succeeded by the deposition of a 120 nm layer of Au onto the SiN coating. Subsequent to this, the Au-coated surface underwent the application of a positive photoresist layer, upon which the deep-UV lithography process was conducted. Upon the completion of the lithography, the gold film was subjected to dry etching, utilizing a gas mixture of SF_6 and Ar. This etching process was undertaken to create the nanoholes within the gold layer. Concluding the procedure, any residual photoresist was removed from the surface through oxygen (O_2) plasma cleaning. The final step encompassed the segmentation of the wafer housing the nanohole apertures throughout its entirety, resulting in the production of plasmonic chips measuring 2 cm × 1 cm in dimensions. Figure 2B-inset shows the scanning electron microscope (SEM) image depicting the nanohole arrays.

Figure 2B shows the optical behavior of the nanohole arrays. The transmission resonance is observed at ~ 635.83 nm. As shown in the literature, this resonance is a consequence of surface plasmon excitations at the top surface of the Au film, occurring at the interface between Au and air, which pertains to the Au/Air(-1,0) mode [28]. Here, we performed finite-difference time-domain (FDTD) simulations, where we employed periodic boundary conditions along the xy-plane to replicate the array's behavior, and a perfectly matched layer was utilized along the propagation direction (z-axis). As shown in Fig. 2B-inset, polarization is along the x-axis and the direction of propagation is along the z-axis. Here, for the imaging module, an unpolarized LED light source was employed, while for simplicity in the FDTD simulations, we utilized an x-polarized light. The nearfield calculation of magnetic field unveils the nature of the transmission resonance, which combines both localized and propagating surface plasmons (Fig. 2C-top). The magnetic field distribution corresponding to this mode displays

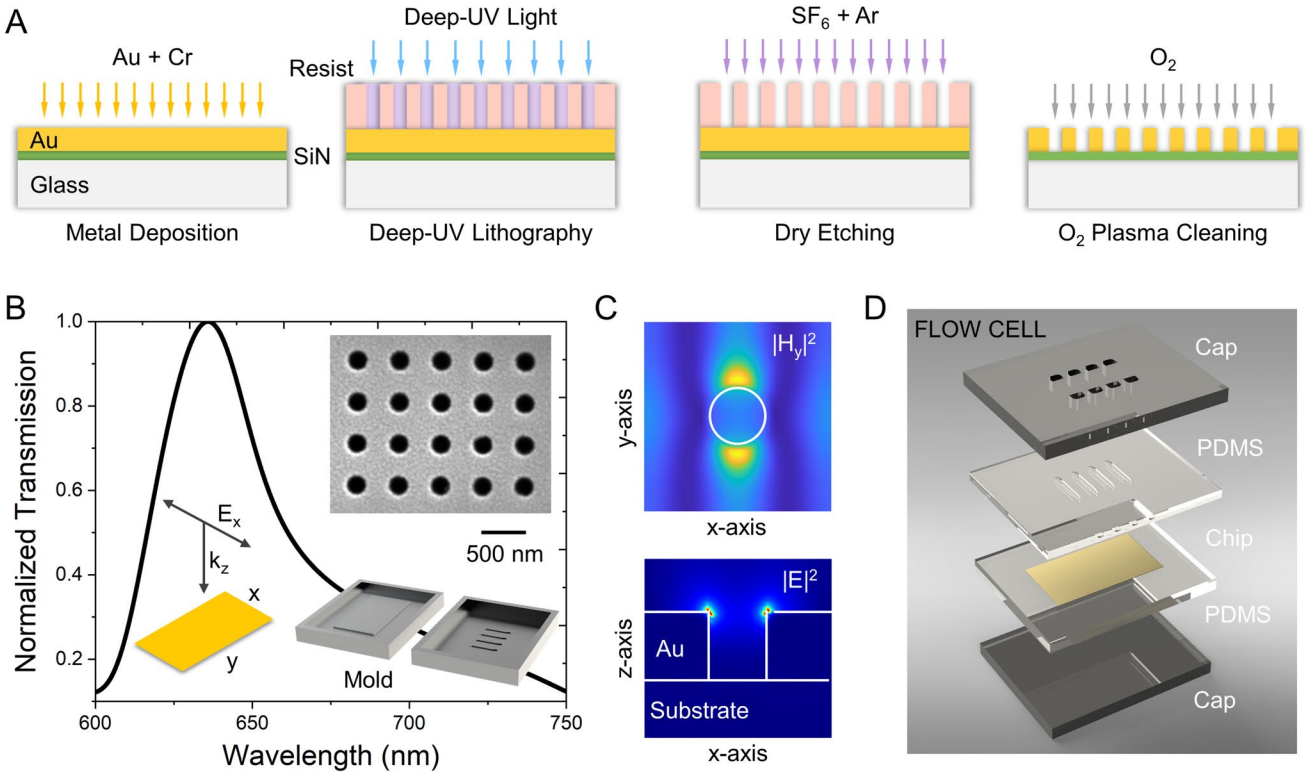

Fig. 2 **A** Sequential stages encompassing the high-throughput fabrication methodology based on deep-UV lithography. **B** The transmission spectrum exhibited by the nanohole arrays under an unpolarized white light source. Insets: Incident light source's polarization and propagation directions used in the FDTD simulations. Additionally, schematic representation of the resin-based 3D printed mold and SEM image of the nanohole arrays. **C** Top: y-component of the magnetic field intensity calculated at the top surface of the Au film. Bottom: Cross-section profile of the electric field intensity. **D** Schematic illustration outlining the constituent components of the flow cell

two symmetric standing field patterns along the x-axis, which signifies the presence of two counter-propagating surface plasmons. Additionally, the aperture rims manifest two points of high intensity, attributed to localized surface plasmons along the y-axis. The electric field distribution (Fig. 2C-bottom) affirms the dipolar character of the mode, revealing concentrated field enhancements around the nanohole rims. These local fields, centered on the upper gold surface's rims, extend into the adjacent medium, thereby rendering them accessible to analytes captured on the gold sensing surface. Importantly, it is worth noting that the subwavelength nanoholes possess a circular configuration, showcasing symmetry across all directions. Given this, an unpolarized LED source was engaged in the imaging module. This design choice ensures the uniform concentration of local fields along the rims, leading to heightened sensitivities in comparison to those achieved with a polarized incident field.

Sample Preparation Module

The sample preparation module comprises two principal components: (i) a piezoelectric pump and (ii) a flow cell. As shown in Fig. 1B, the piezoelectric pump (Bartels Mikrotechnik GmbH, mp6-liq) encompasses a driver board (Bartels Mikrotechnik GmbH, mp6-EVA) driven by a microcontroller (Arduino). The micro-controller-based driver board permits the regulation of diverse flow rates by adjusting the piezoelectric pump's supply voltage within the range of 1.0 to 4.5 V. The micro-controller utilizes pulse-width modulation (PWM) to generate pulses of varying width, representing the amplitude of an analog signal used as input for the driver board. The piezoelectric pump's frequency remained consistent at 100 Hz, ensuring that the linear correlation between voltage and flow rate remained unaffected by frequency fluctuations. The PWM signal originating from the micro-controller is amplified by the driver board to operate the piezoelectric pump. The micro-controller enables the precise linear control of the flow rate through modulation of the input voltage.

For consistency and reproducibility of sensing data, we followed the strategy of the targeted delivery of analytes. Along this line, we used a flow cell equipped with four microfluidic channels for control and sensor testing purposes. Two control channels play a crucial role in eliminating noise stemming from biological, optical, or mechanical

variations. Our flow cell design involves a dual-layer structure composed of polydimethylsiloxane (PDMS). The top PDMS layer houses the microfluidic channels, while the bottom PDMS layer features a rectangular groove sized to accommodate the plasmonic chip. The molds essential for crafting these PDMS layers were produced using resin-based 3D printing (Fig. 2B-inset). Ordinarily, PDMS-based components are affixed to the sensing surface, limiting their reusability. To counteract this constraint, we developed a holder for the flow cell. This holder is composed of two acrylic caps, engineered to establish a leak-proof microfluidic system without necessitating PDMS bonding. Figure 2D illustrates this design approach, where two transparent acrylic caps serve to secure the PDMS layers. The top cap has eight holes aligned with inlets and outlets of the top PDMS layer. To ensure stability and leak-free functionality, four screws were employed to fasten the PDMS layers together, concurrently safeguarding the integrity of the glass slide from any potential fractures.

Illustrated in Fig. 3A, the flow cell consists of four distinct channels designed for the controlled delivery of urine solutions potentially containing NG bacteria, CT bacteria, or a combination of both. These channels direct the solutions to specific regions on the plasmonic chip surface, which has been coated with distinct capturing agents tailored to attract bacteria onto the sensing surface with high specificity. To achieve precise and highly specific bacterial immobilization on the plasmonic chip surface, we performed surface modification through flow cell-assisted functionalization. As described subsequently, we employed a molecular printing system to functionalize the plasmonic pixels designated for control and sensor tests. Additionally, we coated the remaining surface of the plasmonic chip with BSA through a sample preparation module. Within this module, the piezoelectric pump facilitated precise dispensing of BSA (Bovine serum albumin, Thermo Fisher Scientific) and bacteria at a low flow rate over a duration of 20 min. The sequential treatment included protein A/G (Pierce™) binding, followed by antibody attachment, protein BSA coupling, and final bacterial immobilization. Upon completion of these steps, the plasmonic chip was extracted from the flow cell and

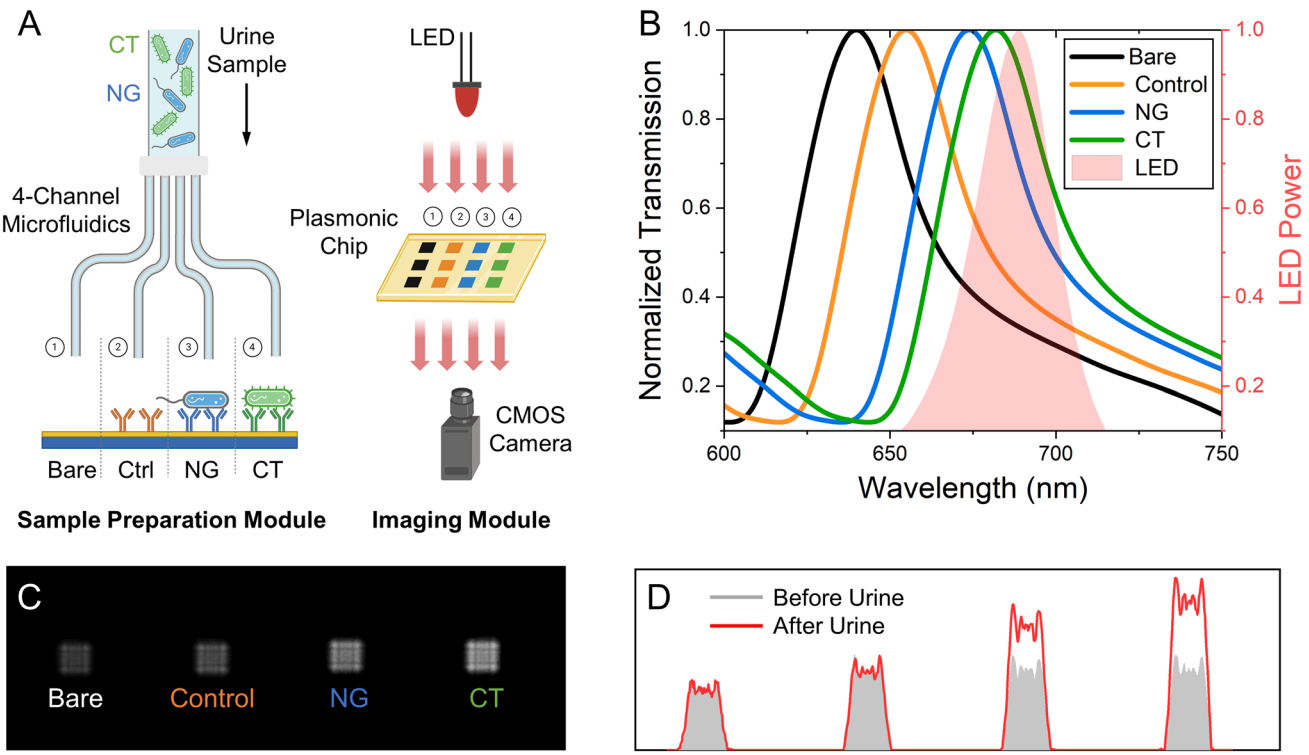

Fig. 3 **A** Schematic illustration of the sample preparation and imaging modules within the portable plasmonic biosensor kit, enabling simultaneous detection of NG and CT bacteria, while employing control regions to ensure testing reliability. Created with BioRender.com. **B** Spectrometer measurements for the transmission resonance supported by the nanohole arrays functionalized with protein A/G (black curve), control antibody (orange curve), 10^6 CFU/mL NG (blue curve), and CT bacteria (green curve), accompanied by the power spectrum of the LED source utilized in the imaging module (red curve). **C** CMOS camera-generated image showcasing the square-shaped plasmonic pixels assigned for protein A/G (labeled as bare), control antibody (orange), NG (blue), and CT (green) bacteria. **D** Variation within diffraction field intensity pre- (gray line) and post-introduction (red line) of a urine sample containing both NG and CT bacteria onto the plasmonic pixels

positioned in front of the CMOS camera within the imaging module for subsequent analysis and imaging.

Imaging Module

The core operating principle of the portable biosensor revolves around capturing diffraction field images emanating from the plasmonic chip through a CMOS camera (Thorlabs, DCC1545M), facilitated by LED illumination, as visually depicted in Fig. 3A. It aims to ascertain spectral fluctuations within the transmission resonance supported by nanohole response by monitoring alterations in intensity prior to and following analyte binding. The limit of detection of the system, denoting the minimal detectable bacteria concentration, corresponds to the lowest bacteria concentration capable of inducing a discernible change in the diffraction field intensity, detectable by the CMOS camera. Consequently, careful selection of the LED light source and CMOS camera becomes imperative, ensuring the capability to induce and monitor changes in diffraction field intensity, even in the presence of exceedingly low bacteria concentrations.

Figure 3A visually delineates constituent elements of the imaging module. As schematically illustrated in Fig. 1B, the lower part, made from PLA (polylactic acid) material, houses the USB-powered CMOS camera, while the upper PLA part integrates the battery-powered LED light source. An inter-PLA tube was incorporated to establish uniform LED illumination across the CMOS's active region. The upper PLA section comprises a circuit comprising a battery, an on/off switch for the light source, and a resistor to modulate LED brightness and avert camera saturation. Within the lower PLA segment, the plasmonic chip could be positioned within a rectangular groove (with the size of the plasmonic chip), harmonizing sensor and control regions with the CMOS camera's active area. The designated square regions allocated for control and sensor testing purposes will be referred to as "plasmonic pixels" throughout the entirety of this article. The square groove also features an oval-shaped indentations for chip manipulation.

The proper selection of components hinges on two crucial factors: (i) the LED source must exhibit a narrow bandwidth and situate spectrally proximate to the nanohole transmission response, and (ii) the CMOS camera necessitates a substantial quantum efficiency encompassing the spectral range encompassing both the transmission signal and LED response. Consistent with previous indications, the chip surface was initially subjected to protein A/G functionalization to ensure proficient binding of analytes and bacteria. Following the A/G functionalization step, a notable shift in transmission resonance was observed, measuring ~ 4 nm, specifically ~ 639.91 nm (Fig. 3B, black curve labeled as bare). The LED source was strategically positioned at ~ 688.65 nm (Digi-Key Electronics, MTE6800N2), maintaining a spectral separation of ~ 33 nm from the transmission resonance of the nanohole arrays (Fig. 3B, red curve). This positioning was chosen to achieve spectral overlap with the transmission resonance across various functionalization stages, including protein A/G, antibody, and bacterial interactions. The quantum efficiency of the CMOS camera demonstrates uniformity within the pertinent spectrum (not shown in the figure). A narrow LED source bandwidth (~ 28 nm) and the CMOS camera's consistent quantum efficiency within the relevant spectrum critically underpin the generation of reliable diffraction field intensity variations, even in the presence of exceedingly minute analyte concentrations.

Results

Detection of NG and CT Bacteria with Plasmonic Imaging

In this study, we conducted a targeted approach for the direct identification of pathogenic bacteria present in urine samples. To achieve this, specific antibodies (anti-NG and anti-CT, Abcam) were strategically utilized to selectively recognize the outer membrane proteins of Neisseria gonorrhoeae (NG, ATCC) and Chlamydia trachomatis (CT, ATCC) bacteria. To ensure accurate bacterial capture facilitated by these antibodies, we employed a recombinant fusion protein known as protein A/G. This fusion protein integrates binding domains from both protein A and protein G, enhancing its affinity for the Fc region of the antibodies associated with the aforementioned bacteria. The utilization of this protein A/G fusion enabled us to create a functional coating on the detection surface. This surface coating, in turn, facilitated the optimal presentation of antibodies in a Y-shaped configuration, thereby exposing their antigen-binding sites in a manner conducive to precise bacterial capturing. This methodology resulted in a significantly elevated level of specificity and selectivity in capturing the target bacteria, offering a robust approach for the accurate detection of NG and CT bacteria within urine samples [29].

Culturing CT bacteria presents unique challenges due to its obligate intracellular nature. Unlike traditional bacteria, it requires living host cells for replication. To initiate the process, McCoy cells were grown to confluency in an appropriate cell culture medium. Following removal of antibiotics from the medium, CT was introduced to the host cells, attaching and initiating infection. Over the course of 48–72 h in an incubator, characteristic inclusion bodies form within the host cells, signifying successful infection [30]. NG bacteria were grown on Thayer–Martin agar in an enriched carbon dioxide atmosphere [31]. For the purpose of optimization, purified and inactivated bacteria were

utilized, where 10% formalin was user for a deactivation. This methodology maintains the integrity of the bacteria's outer membrane structure, which allows for the possibility of capturing the bacteria using their antibodies.

For achieving highly sensitive bacterial detection through our plasmonic methodology, we initiated the process by functionalizing protein A/G and IgG using a molecular printing system. Additionally, we coated the remaining areas of the gold surface with BSA. This strategic modification allowed for effective bacterial capture exclusively on the designated plasmonic pixels, preventing binding to regions beyond the specified plasmonic chip surface areas, as well as other microfluidic components, e.g. inside of the piezoelectric pump and tubings. Consequently, our approach enabled successful sensing signal generation even when dealing with extremely low bacterial concentrations. This accomplishment holds significant relevance in medical applications, as it facilitated the creation of sensing signals within concentrations that are medically pertinent [32].

In our platform, we implemented a microfluidic system featuring four distinct channels, each serving a specific purpose within our experimental framework. For baseline assessment and unspecific binding evaluation, we designated one channel exclusively for a baseline test. This channel was treated with protein A/G and BSA coating only (labeled as bare), allowing us to assess any optical or mechanical fluctuations that could potentially impact the reliability of our results. Furthermore, this channel played a pivotal role in quantifying the contribution of non-specific binding effects. We have an additional channel that was functionalized with a control antibody (labeled as Control, Sigma-Aldrich), demonstrating no affinity for either NG or CT bacteria. This channel was assigned to account for nonspecific binding, thus demonstrating the elevated selectivity and specificity of the antibodies utilized for detecting NG and CT bacteria. An independent sensor channel was exclusively reserved for CT detection (labeled as CT). This channel was functionalized with the antibody dedicated to CT bacteria, facilitating a focused and precise identification process for this pathogen. Similarly, a distinct channel was allocated for the exclusive detection of NG bacteria (labeled as NG). In alignment with the CT channel, this NG-specific channel was functionalized with the antibody tailored to identify NG, thus enabling a parallel and specific analysis. This microfluidics-based approach allowed us to perform targeted investigations, assess specificity, gauge selectivity, and carry out independent detection of CT and NG, collectively contributing to a comprehensive and nuanced understanding of our experimental outcomes.

Figure 3C displays the intensity values corresponding to individual plasmonic pixels designated for different functionalities: protein A/G, control, NG, and CT bacteria, as observed in the CMOS images. Notably, a pronounced spectral shift within the transmission resonance is evident in sensor regions housing bacteria, setting them apart from the control pixels, e.g., antibody (orange curve): ~ 19 nm, NG bacteria (blue curve): ~ 38 nm, CT bacteria (green curve): ~ 46 nm. In Fig. 3D, the initial intensity of the diffraction field is represented by the gray line. This line corresponds to pixels coated with plain protein A/G, and those functionalized with respective antibodies, e.g., control antibody, anti-NG, and anti-CT. Following the introduction of the urine sample containing 10^6 CFU/mL of NG and CT bacteria (represented by the red line), distinctive changes in the diffracted field intensity become apparent. As expected, minimal variation in diffracted field intensity is observed for the bare plasmonic pixel, primarily due to the absence of a capturing mechanism on the surface. Similarly, the control antibody-coated pixel shows negligible intensity variations due to the lack of affinity for both NG and CT bacteria. In contrast, a noticeable increase in diffraction field intensity is observed for the NG and CT plasmonic pixels, directly attributed to bacterial attachment on the sensor surface. Furthermore, the larger spectral shift within the transmission resonance for CT, compared to NG bacteria, results in a more pronounced increase in diffraction field intensity for CT bacteria. In summary, the findings from Figs. 3C and 3D collectively illustrate the clear distinctions in intensity values and spectral shifts, underscoring the successful bacterial attachment and their multiplexed detection via our plasmonic biosensor kit.

System LoD for NG and CT Bacteria

By subjecting samples spiked with NG (Fig. 4A) and CT (Fig. 4B) bacteria to a spectrum of concentrations spanning 10 to 10^6 CFU/mL through tenfold dilutions, we constructed standard calibration curves. We utilized a high protein A/G and antibody concentration, such as 50 µg/mL, to effectively capture bacteria even when they are present in low concentrations. In order to assess the sensitivity and specificity of our biosensor for bacteria quantification, we concentrated on individually detecting CT and NG bacteria within synthetic urine, which was designed to replicate real urine conditions.

To ensure the reliability of each test, every microfluidic channel is equipped with three plasmonic pixels, all functionalized with the same capturing agent. This design allows for repeated testing of the same solution, enhancing the confidence in the results. In the figure, the squares represent the means of three data points obtained for the same concentration. The error bars correspond to twice the standard deviation of three plasmonic pixels located on the same microfluidic channel within the flow cell. These samples were evaluated using plasmonic pixels that were initially coated with anti-CT and anti-NG antibodies. Emanating from this approach, the diffraction field intensity

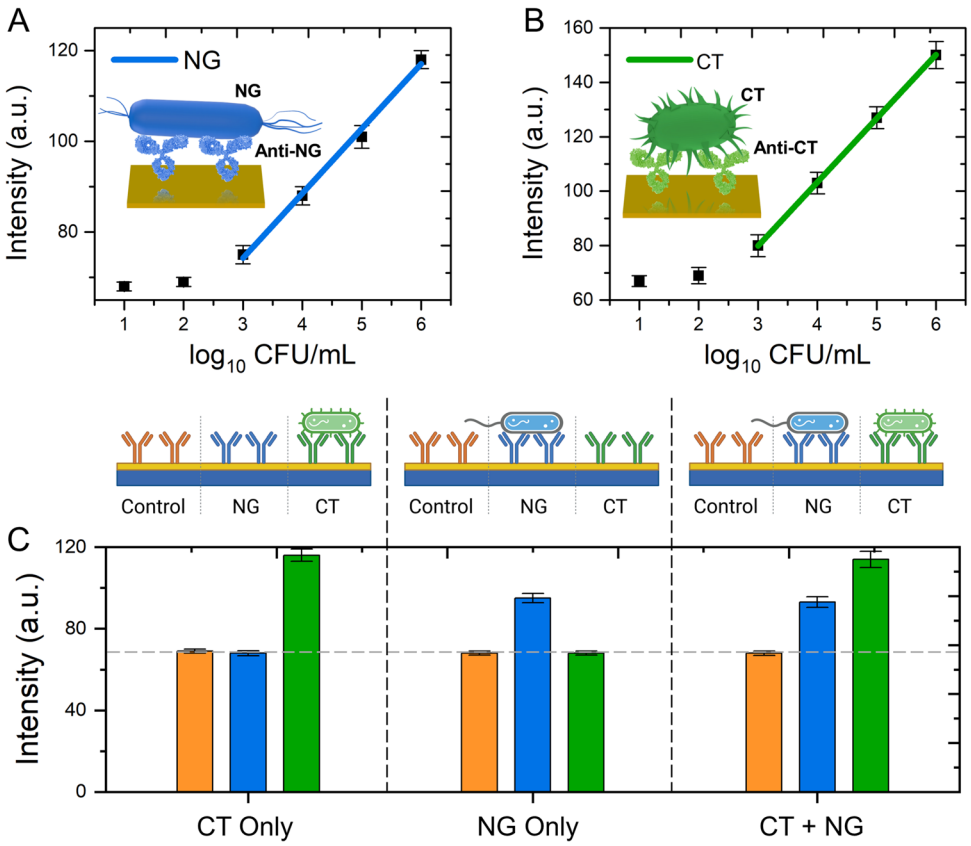

Fig. 4 Calibration curves for **A** NG and **B** CT bacteria within the bacterial concentration range of 10 to 10^6 CFU/mL in urine samples. **C** Diffraction field intensity values determined for urine samples containing only CT bacteria (left figure: green bar), NG bacteria (middle, blue bar), or both (right figure: blue and green bars), where the bacterial concentration is 10^5 CFU/mL (orange bards, control antibody). Bars are the mean values of three experiments and the error bars are twice the standard deviation. Created with BioRender.com

values were collected. Remarkably, an ascending trend in intensity manifested as a function of bacteria concentration. This augmentation in intensity closely aligned with the interplay between the specific bacteria and their corresponding antibodies, underscoring the intrinsic connection between the two factors. Applying the data to a linear regression model yielded $R^2 = 0.99474$ and $R^2 = 0.99987$ for NG and CT bacteria, enabling us to establish the Limit of Detection (LoD) of our biosensor. System LOD was calculated from, $\text{LOD} = 3.3\sigma/\text{s}$, where σ is the standard deviation of the signal and s is the slope of the calibration curve [33, 34]. We determined LOD as 452 CFU/mL for NG bacteria and 121 CFU/mL for CT bacteria. The detection limits were deemed highly satisfactory for diagnostic purposes, as they encompass the physiological concentration range typically encountered in the majority of infection cases [35].

Figure 4C depicts the diffraction field intensity values under three distinct scenarios: urine samples containing solely CT bacteria (left), solely NG bacteria (middle), and a combination of both bacteria strain (right), with the chosen bacterial concentration set at 10^5 CFU/mL. The bars correspond to the mean values of three experiments for the same sample. The error bars represent twice the standard deviation calculated from three plasmonic pixels situated within the same microfluidic channel of the flow cell. As shown in the figure, successful differentiation of bacterial presence was achieved. No discernible response was observed from the control antibody (orange bars) or the antibody with affinity for the alternate bacteria (blue bars: NG bacteria, green bars: CT bacteria). Furthermore, even under elevated bacterial concentrations, such as 10^5 CFU/mL, our imaging-based readout methodology remained unimpaired by nonspecific binding effects.

Software Module

To evaluate the performance of the plasmonic chip using the CMOS camera and transmit sensing data to end-users via image processing, we developed a Python™-based graphical user interface (GUI). This software, depicted in Fig. 5, provides direct access to camera settings (e.g., exposure time and gain) and piezo pump settings (e.g., flow rate and flow duration), allowing operators to fine-tune the test parameters. The plasmonic chip is first positioned inside the flow cell, and the software interfaces with the pump settings. The operator then flowed the chip surface with protein BSA and then urine, where the plasmonic pixels were initially functionalized with protein A/G and IgG via a molecular printing system. Following this functionalization step, the plasmonic chip is removed from the flow cell, and placed in front of the CMOS camera. Through the GUI, operator visualizes the diffraction image, showcasing distinct control and sensor

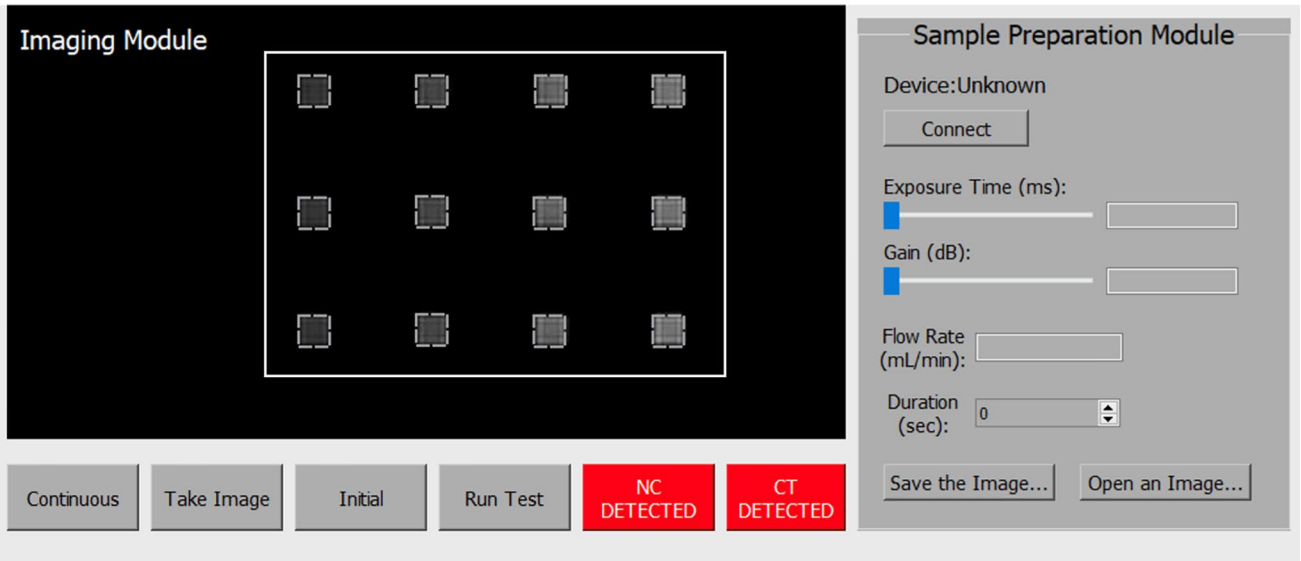

Fig. 5 Software module of the portable plasmonic biosensor kit

areas. By capturing an image and activating the test, the GUI calculates the average diffraction intensity within white dashed squares shown in the figure.

Moreover, the GUI normalizes the average diffraction field intensity values associated with control antibody, NG and CT bacteria. Leveraging calibration data, we determined normalized intensity value ranges for NG and CT bacteria using the control antibody response. The GUI employs the sensor-to-control diffraction field intensity ratio from the CMOS image. If the calculated value falls within these established ranges, the GUI signals bacterial detection to the operator. This methodology minimizes external interference by focusing on diffraction field intensity images of the control region, ensuring data relevance to the targeted analytes. Furthermore, the values corresponding to the control antibody, NG, and CT bacteria were crucially normalized by the response of the bare plasmonic pixel (located on the left, coated with protein A/G and BSA as explained earlier) to eliminate background signal effects. With its user-friendly interface, this program holds considerable promise for field applications, obviating the need for highly trained personnel.

Conclusion

In conclusion, this article introduced a portable plasmonic biosensor kit designed for the detection of Chlamydia trachomatis (CT) and Neisseria gonorrhoeae (NG) in urine samples. This advanced platform integrates label-free sensing technology that utilizes plasmonic nanoholes, coupled with lens-free computational imaging, thus enabling efficient point-of-care diagnosis of pathogenic infections. The system adeptly captures and evaluates diffraction field images, deciphering crucial bacteria-related information through tracking of their variations. Employing a cost-effective pump compartment and a flow cell, the technology ensures precise delivery of samples to the plasmonic chip surface. Supported by a system software, the system facilitates hardware configuration, test execution, and image analysis, culminating in the determination of bacterial presence within urine samples. Leveraging the prowess of both control and sensor antibodies, the technology guarantees exceptional sensitivity and selectivity for the precise detection of bacteria. By employing distinct microfluidic channels equipped with multiple sensor locations, individualized testing for each bacteria type is made possible. Embracing an imaging-centric approach, our technology offers simultaneous detection capabilities for CT and NG bacteria on a unified platform, effectively eliminating the requirement for separate tests. The integration of numerous sensor sites within the microfluidic channels ensures high-throughput testing, further bolstering the robustness of our diagnostic approach. Through the deployment of multiple plasmonic pixels for control assessments, the technology successfully mitigates signals originating from biological, mechanical, or optical sources of noise. The utilization of uncomplicated optics featuring cost-effective components, in conjunction with a controlled environment devoid of the need for intricate optical or mechanical instrumentation, underscores the pragmatic nature of our approach. With its streamlined and lightweight design, and notable limit of detection, such as 452 CFU/mL for NG bacteria and 121 CFU/mL for CT bacteria, our handheld biosensor emerges as a powerful contender for pivotal point-of-care diagnostics within the domain of pathogenic diseases.

Delving into this result, it becomes imperative to contextualize it within the broader landscape of portable biosensors. Compared to previous portable sensor technologies, our plasmonic biosensor exhibits a remarkable leap in detection limits and sensitivity. In order to realize the full potential of our biosensor, it is essential to benchmark it against the gold standard techniques currently employed. This entails a comprehensive assessment of sensitivity, specificity, and reliability when juxtaposed with established diagnostic methods like PCR-based techniques or microbial cultures. Furthermore, it is pertinent to acknowledge that while our technology marks a significant stride toward field-deployable biosensing, there may still be challenges to address, such as potential interference in real-world scenarios, scalability, and the need for extensive validation studies. In light of these considerations, our technology emerges as a transformative advancement with the potential to revolutionize point-of-care diagnostics. With its intrinsic strengths, including high-throughput capabilities, robust detection limits, and the elimination of optical labels, our biosensor could potentially bridge the gap between rapid on-site diagnostics and gold-standard laboratory techniques. While this study brings us closer to the realization of this vision, continued research and development are crucial to refining the technology and tackling any remaining hurdles. As we chart the path ahead, it is the intersection of innovation, rigorous validation, and real-world applicability that will ultimately define the lasting impact of our handheld plasmonic biosensor in the fight against pathogenic diseases.

Author Contribution AEC was responsible for the manufacturing and testing the handheld platform, fabrication, and simulation of the plasmonic chips, performing label-free biosensing tests with bacteria and their interpretations, and developing the system software.

Availability of Data and Materials The data that support the findings of this study are available on request from the corresponding author.

Declarations

Competing Interests The author declares no competing interest.

References

1. Tuddenham S, Hamill MM, Ghanem KG (2022) Diagnosis and treatment of sexually transmitted infections. JAMA 327:161. https://doi.org/10.1001/jama.2021.23487
2. Vallejo-Ortega MT, Gaitán Duarte H, Mello MB et al (2022) A systematic review of the prevalence of selected sexually transmitted infections in young people in Latin America. Rev Panam Salud Pública 46:1. https://doi.org/10.26633/RPSP.2022.73
3. Newman L, Rowley J, Vander Hoorn S et al (2015) Global estimates of the prevalence and incidence of four curable sexually transmitted infections in 2012 based on systematic review and global reporting. PLoS One 10:e0143304. https://doi.org/10.1371/journal.pone.0143304
4. LeFevre ML (2014) Screening for chlamydia and gonorrhea: U.S. preventive services task force recommendation statement. Ann Intern Med 161:902. https://doi.org/10.7326/M14-1981
5. Van Dyck E, Ieven M, Pattyn S et al (2001) Detection of Chlamydia trachomatis and Neisseria gonorrhoeae by enzyme immunoassay, culture, and three nucleic acid amplification tests. J Clin Microbiol 39:1751–1756. https://doi.org/10.1128/JCM.39.5.1751-1756.2001
6. Davidson KW, Barry MJ, Mangione CM et al (2021) Screening for Chlamydia and Gonorrhea. JAMA 326:949. https://doi.org/10.1001/jama.2021.14081
7. Samuel VR, Rao KJ (2022) A review on label free biosensors. Biosens Bioelectron X 11:100216. https://doi.org/10.1016/j.biosx.2022.100216
8. Chen C, Wang J (2020) Optical biosensors: an exhaustive and comprehensive review. Analyst 145:1605–1628. https://doi.org/10.1039/c9an01998g
9. Sumitha MS, Xavier TS (2023) Recent advances in electrochemical biosensors – a brief review. Hybrid Adv 2:100023. https://doi.org/10.1016/j.hybadv.2023.100023
10. Chalklen T, Jing Q, Kar-Narayan S (2020) Biosensors based on mechanical and electrical detection techniques. Sensors 20:5605. https://doi.org/10.3390/s20195605
11. Cooper MA (2002) Optical biosensors in drug discovery. Nat Rev Drug Discov 1:515–528. https://doi.org/10.1038/nrd838
12. Belushkin A, Yesilkoy F, González-López JJ et al (2020) Rapid and digital detection of inflammatory biomarkers enabled by a novel portable nanoplasmonic imager. Small 16. https://doi.org/10.1002/smll.201906108
13. Qavi AJ, Wu C, Lloyd M et al (2022) Plasmonic fluor-enhanced antigen arrays for high-throughput, serological studies of SARS-CoV-2. ACS Infect Dis 8:1468–1479. https://doi.org/10.1021/acsinfecdis.2c00086
14. Hill RT (2015) Plasmonic biosensors WIREs Nanomedicine and Nanobiotechnology 7:152–168. https://doi.org/10.1002/wnan.1314
15. Jackman JA, Linardy E, Yoo D et al (2016) Plasmonic nanohole sensor for capturing single virus-like particles toward virucidal drug evaluation. Small 12:1159–1166. https://doi.org/10.1002/smll.201501914
16. Brolo AG (2012) Plasmonics for future biosensors. Nat Photonics 6:709–713. https://doi.org/10.1038/nphoton.2012.266
17. Masson JF (2020) Portable and field-deployed surface plasmon resonance and plasmonic sensors. Analyst 145:3776–3800. https://doi.org/10.1039/d0an00316f
18. Hamza ME, Othman MA, Swillam MA (2022) Plasmonic biosensors: review Biology (Basel) 11:621. https://doi.org/10.3390/biology11050621
19. Cetin AE, Coskun AF, Galarreta BC et al (2014) Handheld high-throughput plasmonic biosensor using computational on-chip imaging. Light Sci Appl 3. https://doi.org/10.1038/lsa.2014.3
20. Cetin AE, Kocer ZA, Topkaya SN, Yazici ZA (2021) Handheld plasmonic biosensor for virus detection in field-settings. Sensors Actuators B Chem 344:130301. https://doi.org/10.1016/j.snb.2021.130301
21. Coskun AF, Cetin AE, Galarreta BC et al (2014) Lensfree optofluidic plasmonic sensor for real-time and label-free monitoring of molecular binding events over a wide field-of-view. Sci Rep 4:1–7. https://doi.org/10.1038/srep06789
22. Chen X, Zhou Q, Yuan W et al (2023) Visual and rapid identification of Chlamydia trachomatis and Neisseria gonorrhoeae using multiplex loop-mediated isothermal amplification and a gold nanoparticle-based lateral flow biosensor. Front Cell Infect Microbiol 13. https://doi.org/10.3389/fcimb.2023.1067554
23. Wang Y, Knoll W, Dostalek J (2012) Bacterial pathogen surface plasmon resonance biosensor advanced by long range surface

plasmons and magnetic nanoparticle assays. Anal Chem 84:8345–8350. https://doi.org/10.1021/ac301904x
24. Cui J, Zhou M, Li Y et al (2021) A new optical fiber probe-based quantum dots immunofluorescence biosensors in the detection of Staphylococcus aureus. Front Cell Infect Microbiol 11. https://doi.org/10.3389/fcimb.2021.665241
25. Ács N, Gambino M, Brøndsted L (2020) Bacteriophage enumeration and detection methods. Front Microbiol 11. https://doi.org/10.3389/fmicb.2020.594868
26. Yoo SM, Kim D-K, Lee SY (2015) Aptamer-functionalized localized surface plasmon resonance sensor for the multiplexed detection of different bacterial species. Talanta 132:112–117. https://doi.org/10.1016/j.talanta.2014.09.003
27. Soler M, Belushkin A, Cavallini A et al (2017) Multiplexed nanoplasmonic biosensor for one-step simultaneous detection of Chlamydia trachomatis and Neisseria gonorrhoeae in urine. Biosens Bioelectron 94:560–567. https://doi.org/10.1016/j.bios.2017.03.047
28. Yanik AA, Cetin AE, Huang M et al (2011) Seeing protein monolayers with naked eye through plasmonic Fano resonances. Proc Natl Acad Sci 108:11784–11789. https://doi.org/10.1073/pnas.1101910108
29. Yanik AA, Huang M, Kamohara O et al (2010) An optofluidic nanoplasmonic biosensor for direct detection of live viruses from biological media. Nano Lett 10:4962–4969. https://doi.org/10.1021/nl103025u
30. Shao† L, Guo† Y, Jiang Y et al (2016) Sensitivity of the Standard Chlamydia trachomatis culture method is improved after one additional in vitro passage. J Clin Lab Anal 30:697–701. https://doi.org/10.1002/jcla.21924
31. Brendefur Corwin L, Campbell P, Jakobsen K et al (2023) Improvement in Neisseria gonorrhoeae culture rates by bedside inoculation and incubation at a clinic for sexually transmitted infections. Ann Clin Microbiol Antimicrob 22:27. https://doi.org/10.1186/s12941-023-00576-0
32. Huang M, Galarreta BC, Cetin AE, Altug H (2013) Actively transporting virus like analytes with optofluidics for rapid and ultrasensitive biodetection. Lab Chip 13:4841–4847. https://doi.org/10.1039/c3lc50814e
33. Brunetti BDE (2015) About estimating the limit of detection by the signal to noise approach. Pharm Anal Acta 06. https://doi.org/10.4172/2153-2435.1000355
34. Armbruster DA, Pry T (2008) Limit of blank, limit of detection and limit of quantitation. Clin Biochem Rev 29(Suppl 1):S49-52
35. Onorini D, Borel N, Schoborg RV, Leonard CA (2022) Neisseria gonorrhoeae limits Chlamydia trachomatis inclusion development and infectivity in a novel in vitro co-infection model. Front Cell Infect Microbiol 12. https://doi.org/10.3389/fcimb.2022.911818